

Computational Investigation and Design Optimization of a Lateral-Jet-Controlled Missile

Jae-Woo Lee,* Byung-Young Min,† Yung-Hwan Byun,‡ and Yung H. Yu§
Konkuk University, Seoul 143-701 Republic of Korea

To investigate the behavior of normal force and pitching moment characteristics for different angles of attack and spouting jet angles, a parametric study of a lateral-jet-controlled missile has been performed. For this purpose, a three-dimensional Navier–Stokes computer code, AADL3D, has been developed and validated. Based on results of the parametric study, pitching moment and normal force coefficients have been selected as the objective and constraint functions, respectively. The flight Mach number, the angle of attack, and the spouting lateral jet angle are the design variables. With implementation of a genetic algorithm for the global optimum and the response surface method, the design optimization of the lateral-jet-controlled missile has been performed to evaluate the most effective flight conditions for the missile control.

Nomenclature

C_M	= moment coefficient, M/qSd
C_N	= normal force coefficient, N/qS
C_p	= pressure coefficient
C_T	= thrust coefficient, T_{jet}/qS
d	= missile diameter, m
M	= pitching moment, N · m
M_{jet}	= jet Mach number
M_∞	= freestream Mach number
\dot{m}_{jet}	= mass flow rate of jet, kg/s
N	= normal force, N
P_{jet}	= jet pressure
P_{ratio}	= jet pressure ratio, P_{jet}/P_∞
q	= dynamic pressure
S	= missile cross-sectional area, m^2
T_{jet}	= jet thrust, N
α	= angle of attack, deg
θ	= circumferential angle around the missile body, deg
ψ	= spouting jet angle, deg

Subscripts

FL	= forebody lower side of missile
FU	= forebody upper side of missile
jet	= jet-on condition
jetoff	= jet-off condition
M	= moment, N · m
RL	= rear body lower side of missile
RU	= rear body upper side of missile
∞	= freestream condition

Received 10 August 2005; revision received 30 September 2005; accepted for publication 4 October 2005. Copyright © 2005 by the authors. Published by the American Institute of Aeronautics and Astronautics, Inc., with permission. Copies of this paper may be made for personal or internal use, on condition that the copier pay the \$10.00 per-copy fee to the Copyright Clearance Center, Inc., 222 Rosewood Drive, Danvers, MA 01923; include the code 0021-8669/06 \$10.00 in correspondence with the CCC.

*Associate Professor, Department of Aerospace Engineering, Center for Advanced e-System Integration Technology, 1 Hwayang, Gwangjin; jwlee@konkuk.ac.kr. Member AIAA.

†Graduate Research Assistant, Department of Aerospace Engineering, Center for Advanced e-System Integration Technology, 1 Hwayang, Gwangjin. Member AIAA.

‡Professor, Department of Aerospace Engineering, Center for Advanced e-System Integration Technology, 1 Hwayang, Gwangjin. Senior Member AIAA.

§Professor, Department of Aerospace Engineering, Center for Advanced e-System Integration Technology, 1 Hwayang, Gwangjin. Member AIAA.

Introduction

THE lateral-jet-controlled missile possesses high maneuverability by overcoming the delayed response time and the limitations due to the high dynamic pressure requirement of the existing fin-controlled missile. Therefore, the lateral-jet attitude control has been a preferred concept as a new missile defense system.¹ The high-pressure region in front of the nozzle compounded with the low-pressure region behind it generates a complicated flow structure around the lateral-jet-controlled missile producing a pitching down moment around the jet nozzle. This phenomenon leads to inadvertent normal force loss generated by the low-pressure region behind the nozzle, as well as the wraparound effect (Fig. 1) of the separation and bow shocks due to the missile's three-dimensional shape.^{1,2}

Current approaches have shown that these phenomena are affected by parameters such as flight condition, jet nozzle arrangement, jet nozzle shape, jet position, spouting jet angle, and jet flow characteristics such as jet pressure, jet Mach number, and jet mass flow rate.^{3,4} However, further systematic study is required to understand fully the phenomena and trends of the missile behavior with respect to the variation of those parameters to obtain an efficient design of the lateral-jet-controlled missile. Therefore, the effect of angle of attack and spouting jet angle are investigated thoroughly by comparing the normal force coefficient and the moment coefficient. A three-dimensional Navier–Stokes computer code, AADL3D, has been developed and validated for the analysis of the complex lateral jet flow structure. Furthermore, the inadvertent negative effects, such as pitchdown moment and normal force loss, should be minimized. Thus, based on results of the parametric study, a numerical design optimization study for the efficient flight condition is performed.

Aerodynamic Analysis Method

Governing Equations

A three-dimensional Navier–Stokes computer code, AADL3D, is developed for the analysis of complex flow phenomena around the lateral-jet-controlled missile. These equations for the computational domain are shown in Eqs. (1–3). The spatial flux vectors E , F , and G , and viscous terms E_v , F_v and G_v are given by Eq. (2), using contravariant velocities U , V , and W . Thus,

$$\frac{\partial \mathbf{Q}}{\partial t} + \frac{\partial \mathbf{E}}{\partial \xi} + \frac{\partial \mathbf{F}}{\partial \eta} + \frac{\partial \mathbf{G}}{\partial \zeta} = \frac{\partial \mathbf{E}_v}{\partial \xi} + \frac{\partial \mathbf{F}_v}{\partial \eta} + \frac{\partial \mathbf{G}_v}{\partial \zeta} \quad (1)$$

$$\mathbf{Q} = \frac{1}{J} \begin{Bmatrix} \rho \\ \rho u \\ \rho v \\ \rho w \\ e_t \end{Bmatrix}, \quad \mathbf{E} = \frac{1}{J} \begin{Bmatrix} \rho U \\ \rho uU + \xi_x p \\ \rho vU + \xi_y p \\ \rho wU + \xi_z p \\ (e_t + p)U \end{Bmatrix}$$

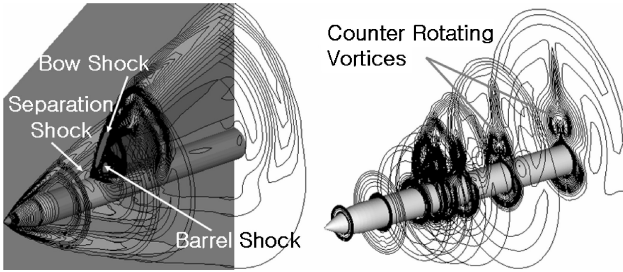


Fig. 1 Complicated flow structure around lateral-jet-controlled missile.

$$\begin{aligned}
 \mathbf{F} &= \frac{1}{J} \begin{Bmatrix} \rho V \\ \rho u V + \eta_x p \\ \rho v V + \eta_y p \\ \rho w V + \eta_z p \\ (e_t + p)V \end{Bmatrix}, \quad \mathbf{G} = \frac{1}{J} \begin{Bmatrix} \rho W \\ \rho u W + \xi_x p \\ \rho v W + \xi_y p \\ \rho w W + \xi_z p \\ (e_t + p)W \end{Bmatrix} \\
 \mathbf{E}_v &= \frac{1}{JRe_a} \begin{Bmatrix} 0 \\ \xi_x \tau_{xx} + \xi_y \tau_{yx} + \xi_z \tau_{zx} \\ \xi_x \tau_{xy} + \xi_y \tau_{yy} + \xi_z \tau_{zy} \\ \xi_x \tau_{xz} + \xi_y \tau_{yz} + \xi_z \tau_{zz} \\ \xi_x \beta_x + \xi_y \beta_y + \xi_z \beta_z \end{Bmatrix} \\
 \mathbf{F}_v &= \frac{1}{JRe_a} \begin{Bmatrix} 0 \\ \eta_x \tau_{xx} + \eta_y \tau_{yx} + \eta_z \tau_{zx} \\ \eta_x \tau_{xy} + \eta_y \tau_{yy} + \eta_z \tau_{zy} \\ \eta_x \tau_{xz} + \eta_y \tau_{yz} + \eta_z \tau_{zz} \\ \eta_x \beta_x + \eta_y \beta_y + \eta_z \beta_z \end{Bmatrix} \\
 \mathbf{G}_v &= \frac{1}{JRe_a} \begin{Bmatrix} 0 \\ \zeta_x \tau_{xx} + \zeta_y \tau_{yx} + \zeta_z \tau_{zx} \\ \zeta_x \tau_{xy} + \zeta_y \tau_{yy} + \zeta_z \tau_{zy} \\ \zeta_x \tau_{xz} + \zeta_y \tau_{yz} + \zeta_z \tau_{zz} \\ \zeta_x \beta_x + \zeta_y \beta_y + \zeta_z \beta_z \end{Bmatrix} \\
 \beta_x &= u \tau_{xx} + v \tau_{xy} + w \tau_{xz} - q_x \\
 \beta_y &= u \tau_{yx} + v \tau_{yy} + w \tau_{yz} - q_y \\
 \beta_z &= u \tau_{zx} + v \tau_{zy} + w \tau_{zz} - q_z
 \end{aligned} \quad (2)$$

In Eqs. (1) and (2), \mathbf{Q} is the conservative variable vector; ρ is the density of the air; p is the pressure; u , v , and w are the velocity components; e_t is the total energy per unit mass; J is the Jacobian from the coordinate transformation; Re_a is the Reynolds number based on the sonic velocity; τ is the shear stress; and q_x , q_y , and q_z are the heat fluxes.

The Spalart–Allmaras one-equation turbulence model is implemented in the AADL3D code, for relatively rapid computational time (see Ref. 5).

Roe's flux difference splitting scheme is implemented for the spatial discretization with use of MUSCL (Ref. 6) for higher-order extension. The minmod limiter⁶ is used to remove solution oscillations. A central difference scheme is used for the calculation of the viscous flux term, whereas the fully implicit lower-upper symmetric Gauss–Seidal algorithm scheme (see Ref. 7) is employed for time integration.

Validation of the Numerical Approach

Ogive–Cylinder Body

To check whether the developed code correctly predicts the supersonic flowfield around the missile body, the calculated surface pressure distributions on an ogive–cylinder body are compared with the experimental measurement results of Perkins and Jorgensen⁸ at angles of attack of 0, 5, and 10 deg. The freestream Mach number

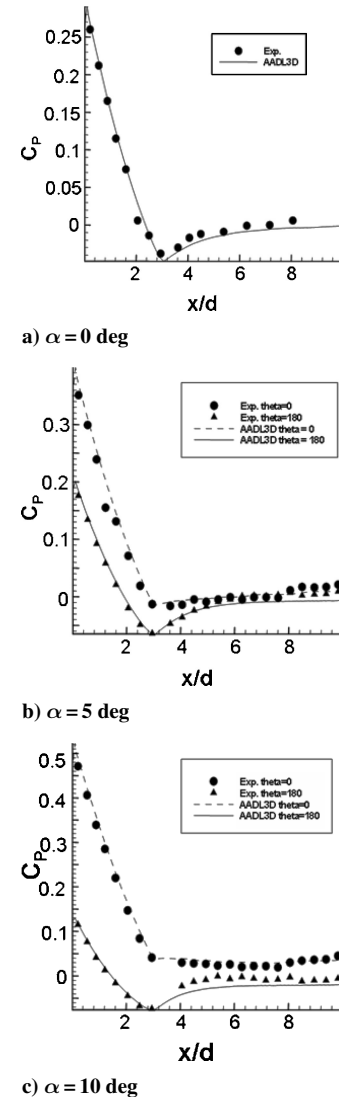


Fig. 2 Comparison of surface pressure coefficients along axial direction, $M_\infty = 1.98$ and $Re = 0.39 \times 10^6$.

and the Reynolds number are 1.98 and 0.39×10^6 , respectively. The computational grid is $70 \times 40 \times 40$ for a half-body.

A comparison of pressure coefficients between the computational results and the experimental data is shown in Figs. 2 and 3. The value along the axial distance is shown in Fig. 2, where $\theta = 0$ deg and $\theta = 180$ deg represent the windward and leeward sides, respectively. The axial distance is nondimensionalized by the diameter of cylinder. The value along the circumferential angles between 0 and 180 deg is shown in Fig. 3. At an angle of attack of 10 deg, the numerically predicted separation point is a little different from the experimental data at the leeward side, but at the windward side and near the nose, the agreement is excellent. Overall computational results are in good agreement with the experimental data.

Missile Body with Lateral Jet

The results of AADL3D code analysis, incorporating both angle of attack and lateral jet, are compared with existing calculation results and wind-tunnel experimental data of Srivastava⁴ to validate the code's accuracy for a three-dimensional missile shape. The freestream Mach number and the Reynolds number are 2.97 and 8.2×10^5 , respectively. The experimental conditions of each case are summarized and compared in Table 1.

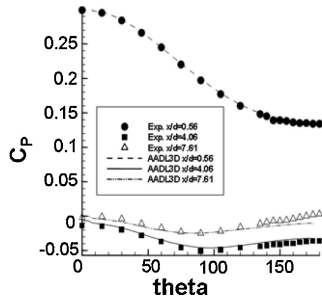
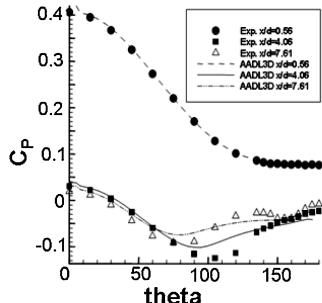
The C_p contours at the symmetry plane for cases 3 and 4 are shown in Fig. 4. The barrel shock and bow shock shapes and different flow phenomena around the jet nozzle can be seen clearly in Fig. 4. When the jet is located at the windward side, the flow separation region in front of the jet nozzle is reduced and the vortices bent

Table 1 Experimental condition⁴

Test case	C_r	Angle of attack, deg	Jet location
1	1.0	20	Leeward jet
2	1.0	20	Windward jet
3	4.0	20	Leeward jet
4	4.0	20	Windward jet
5	Jet off	20	—

Table 2 Normal force coefficient comparison

Test case	C_N		
	Raytheon experiment	Raytheon calculation	AADL3D
1	3.37	2.77	3.20
2	4.64	4.56	4.52
3	0.21	-0.19	0.25
4	7.33	7.27	7.35
5	4.36	3.73	4.15

a) $\alpha = 5$ degb) $\alpha = 10$ deg**Fig. 3 Comparison of surface pressure coefficients along circumferential direction, $M_\infty = 1.98$ and $Re = 0.39 \times 10^6$.**

by the freestream are wrapped around the missile body. Moreover, the propagated vortices hit the missile body downstream, generating another high-pressure region. AADL3D results are compared with the Raytheon calculations and experimental results in Table 2. AADL3D provides better normal force prediction than Srivastava.⁴

Parametric Studies of Lateral-Jet-Controlled Missile

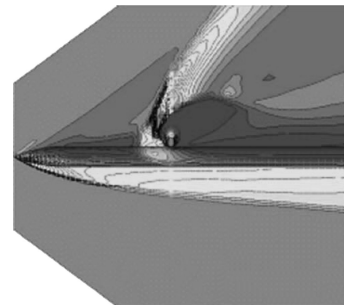
Grid System Selection

The missile configuration for the case studies is a simple tangent ogive–cylinder body without a fin, as shown in Fig. 5. A grid system that is coarse but guarantees solution accuracy is selected by investigating the convergence rate and the converged solutions of several grid systems. This grid system also leads to greater computational efficiency. The chamber condition of the lateral jet and the inside contour of the jet nozzle effects are ignored to facilitate analyses. Thus, the lateral jet flow condition is set on the nozzle exit plane as a fixed boundary condition.

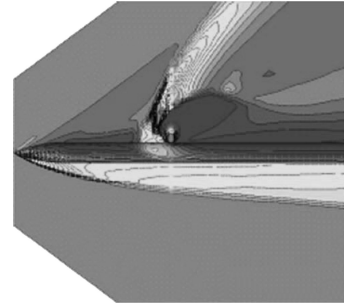
The freestream Mach number is 2.6, and the jet Mach number is 2.04. P_{ratio} is 45.7 and the Reynolds number is 6.63×10^6 . The 10-km standard atmospheric condition is used as the ambient condition. For an optimum combination of computational time and accuracy, the $95 \times 34 \times 33$ (streamwise 95, circumferential 34, and surface normal direction 33) grid system containing 106,590 cells is

Table 3 Analysis conditions for angle-of-attack effect study

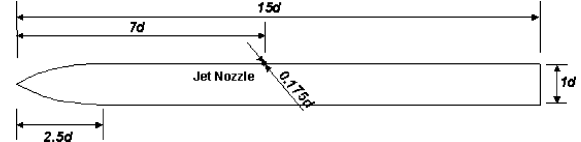
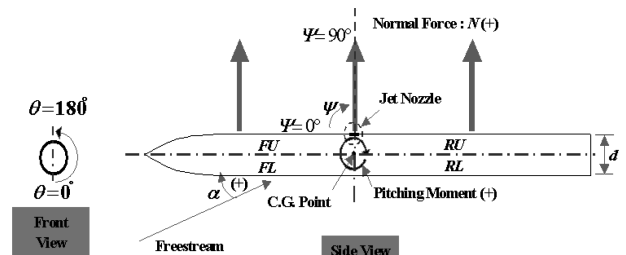
Parameter	Case 1	Case 2	Case 3	Case 4	Case 5
P_{ratio}	45.7	45.7	45.7	45.7	45.7
M_{jet}	2.04	2.04	2.04	2.04	2.04
M_∞	2.6	2.6	2.6	2.6	2.6
α , deg	-20	-10	0	10	20
ψ , deg	90	90	90	90	90
θ_{jet} , deg	180	180	180	180	180



a) Case 3



b) Case 4

Fig. 4 C_p contour at symmetry plane.**Fig. 5 Missile configuration for case studies.****Fig. 6 Nomenclature definitions.**

selected. Approximately 6 ~ 9 points are included inside the boundary layer.

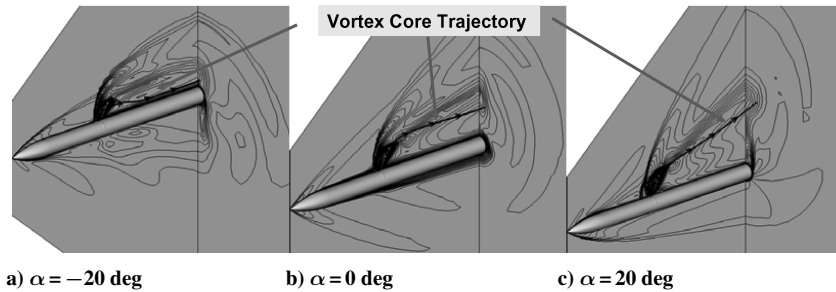
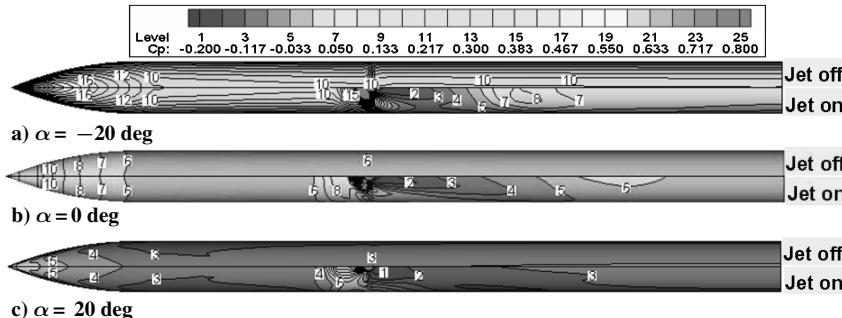
Analysis Conditions and Nomenclature Definitions

The analysis conditions, except for angle of attack and spouting jet angle, of the freestream flow and lateral jet are kept the same, as is the grid system selection, in all calculations. To determine the freestream–jet angle effect, case studies have been performed for five different angles of attack and seven spouting jet angles. Each analysis condition is summarized in Tables 3 and 4.

The missile configuration is nondimensionalized by the missile diameter d . Force, moment, and other parameters are defined in Fig. 6. The missile surface was divided into four regions with respect

Table 4 Analysis conditions for spouting jet angle effect study

Parameter	Case 6	Case 7	Case 8	Case 9	Case 10	Case 11	Case 12	Case 13
P_{ratio}	45.7	45.7	45.7	45.7	45.7	45.7	45.7	45.7
M_{jet}	2.04	2.04	2.04	2.04	2.04	2.04	2.04	2.04
M_∞	2.6	2.6	2.6	2.6	2.6	2.6	2.6	2.6
α , deg	0	0	0	0	0	0	0	0
ψ , deg	30	45	60	75	90	105	120	135
θ_{jet} , deg	180	180	180	180	180	180	180	180

**Fig. 7** Mach number contour and vortex core transmission.**Fig. 8** C_p contour on surface.

to the center of gravity, and the normal force and moment distribution for each region were compared.

Angle of Attack Effect

Vortex Formation

Mach number contour and vortex core transmission, generated from freestream–jet interaction for angles of attack of -20 , 0 , and 20 deg, are shown in Fig. 7. At $\alpha = 20$ deg, the upper-side vortex generated by the jet deviates farthest from the surface. As a result, the influence of the vortex on the missile surface is relatively small. In contrast, at $\alpha = -20$ deg, the generated vortex is bent by the freestream causing it to sweep the missile surface. This bending of the vortex protects the missile surface from the downward freestream impact. Therefore, the strong bow shock effect caused by the downward freestream velocity component is removed from the upper rear body surface, whereas a larger low-pressure region is formed in comparison to the jet-off case.

Pressure, Normal Force, and Pitching Moment

Pressure contours on the missile surface are shown in Fig. 8. It can be shown that a relatively stronger secondary shock is generated farther upstream of upper rear body surface at $\alpha = -20$ deg than at $\alpha = 0$ deg because of the vortices bent by the downward freestream. To reiterate, no secondary shock occurs at $\alpha = 20$ deg. Furthermore, the strong bow shock in front of the jet nozzle at the negative angle of attack (the windward jet) leads to an increase in the normal force. In spite of rising pressure caused by a secondary shock at the upper rear body surface at $\alpha = -20$ deg, a lower pressure distribution is obtained near the region behind jet when compared to the jet-off case. This pressure distribution is attributed to the blocking of the influence of the strong bow shock by the bent vortices. Therefore,

the freestream–jet interaction causes a greater normal force loss and pitchdown moment. In contrast, for $\alpha = 20$ deg, there is very little difference in pressure distribution between the jet-off and the jet-on cases. The normal force and the pitching moment coefficients caused by jet effect for different angles of attack are shown in Table 5 and Fig. 9.

As shown in Table 5 and Fig. 9, a negative angle of attack (windward jet), contrary to the positive angle of attack (leeward jet), causes a relatively greater normal force loss and pitchdown moment. This is primarily due to the large region of low pressure created behind the nozzle, as shown in Table 5. Furthermore, a high degree of non-linear behavior is observed in the normal force and the pitching down moment by the jet for different angles of attack, especially near highly negative angles of attack.

Spouting Jet Angle Effect

The attitude control method considered in this study using a lateral jet is for obtaining a transition movement of the missile by locating the jet at the missile center of gravity to avoid pitching moment generation. Cases 1–5 showed that the shock interaction effect causes a pitching down moment around the jet nozzle. The low-pressure region formed by the effects of suction and the vortex at the rear upper body surfaces is the primary factor in the pitching down moment generation. An inference can be drawn here that inclining the jet more steeply, coupled with a greater separation of the propagated vortex from the missile surface, leads to a reduction in the suction and vortex effects. This reduction causes the pitching down moment to decrease. Thus, a forward inclined spouting jet angle would achieve this effect easily. In this study, several spouting jet angles ($\psi = 30, 45, 60, 75, 90, 105$, and 120 deg) have been analyzed and their results are compared.

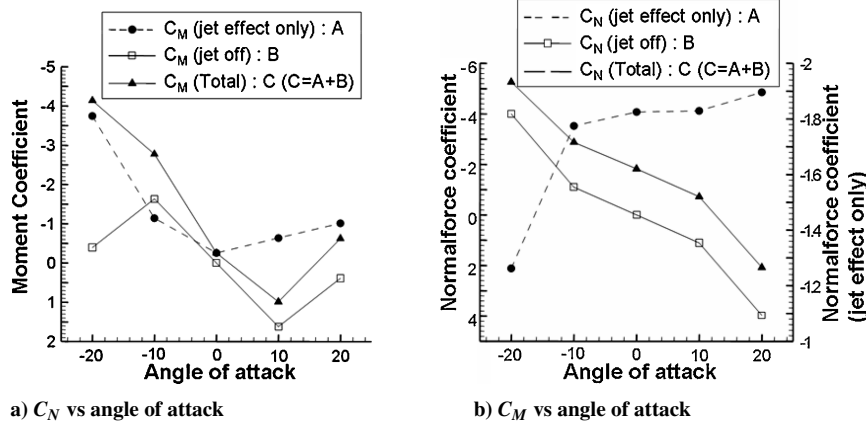
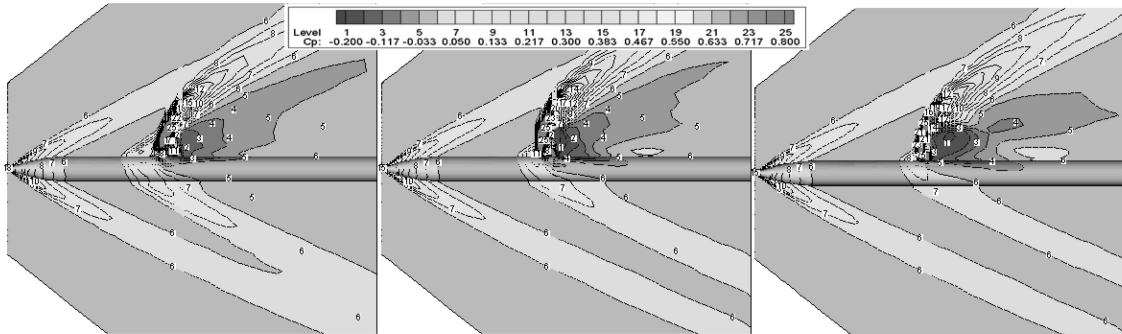
Table 5 Comparison of calculated results for angle of attack effect^a

α , deg	C_N	$C_{N_{FU}}$	$C_{N_{FL}}$	$C_{N_{RU}}$	$C_{N_{RL}}$	C_M	$C_{M_{FU}}$	$C_{M_{FL}}$	$C_{M_{RU}}$	$C_{M_{RL}}$
20	-1.896	-0.203	0.007	0.284	0.032	-1.011	-0.102	0.002	-0.836	-0.075
10	-1.829	-0.167	0.035	0.256	0.064	-0.636	-0.124	0.013	-0.591	0.066
0	-1.825	-0.171	0.041	0.321	0.	-0.255	-0.079	0.017	-0.543	0.351
-10	-1.775	-0.227	0.027	0.448	-0.006	-1.140	-0.060	0.010	-1.080	-0.010
-20	-1.262	-0.287	0.018	0.944	0.080	-3.745	-0.073	0.006	-3.148	-0.529

^aJet effect only is equal to the total value minus the angle-of-attack effect.

Table 6 Spouting jet angle effect results

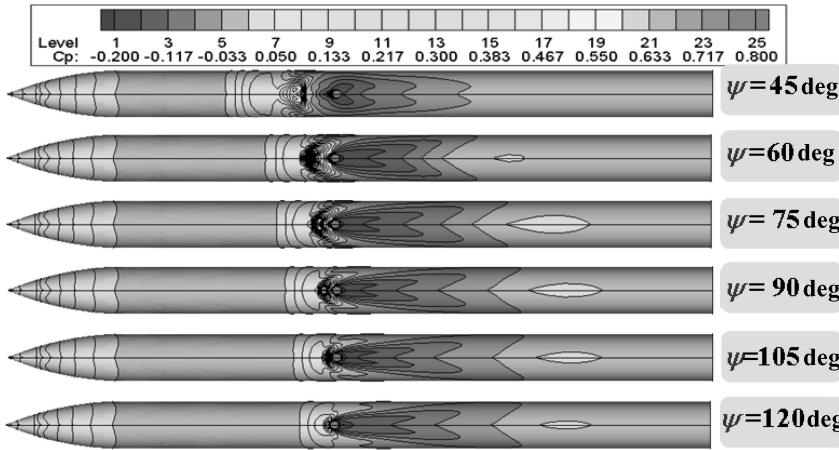
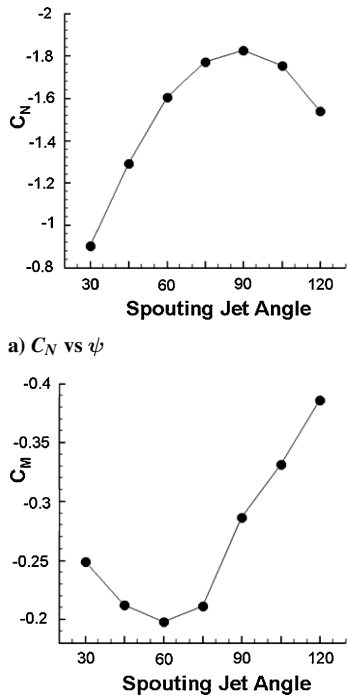
ψ , deg	C_T	C_N	$C_{N_{FU}}$	$C_{N_{FL}}$	$C_{N_{RU}}$	$C_{N_{RL}}$	C_M	$C_{M_{FU}}$	$C_{M_{FL}}$	$C_{M_{RU}}$	$C_{M_{RL}}$
30	1.008	-0.901	-0.274	0.230	0.256	-0.104	-0.249	-0.515	0.304	-0.527	0.489
45	1.426	-1.291	-0.270	0.223	0.277	-0.094	-0.212	-0.461	0.262	-0.510	0.497
60	1.746	-1.604	-0.243	0.092	0.298	-0.004	-0.198	-0.174	-0.051	-0.427	0.352
75	1.948	-1.771	-0.210	0.064	0.322	0.0	-0.211	-0.118	0.029	-0.490	0.367
90	2.016	-1.825	-0.161	0.042	0.313	-0.002	-0.286	-0.077	0.014	-0.554	0.331
105	1.948	-1.754	-0.123	0.024	0.296	-0.003	-0.331	-0.053	0.011	-0.556	0.267
120	1.746	-1.540	-0.081	0.010	0.280	-0.003	-0.386	-0.028	0.003	-0.561	0.200

Fig. 9 C_N and C_M vs angle of attack.Fig. 10 C_P contour on symmetry plane for different spouting jet angle.

The pressure contours at the symmetry plane and on the missile surface are shown in Figs. 10 and 11. A summary of the calculated results is shown in Table 6. The results are shown in Fig. 12. The inclined spouting jet angle in forward direction, as expected, causes a decrease in the low-pressure region behind jet nozzle. This jet angle also leads to a forward extension of the high-pressure region in front of the jet nozzle generated by the bow shock and the separation shock. Furthermore, the high-pressure region, due to the wraparound effect on the opposite side of the jet nozzle, moves forward. From Fig. 12 and Table 6, it can be observed that pitching down moment decreases because the low-pressure region behind the jet nozzle decreases as the spouting jet angle inclines forward.

This low-pressure region is a major factor for the pitching down moment generation. However, an excessively inclined spouting jet angle generates a high-pressure region due to the wraparound effect of bow and separation shocks on the forebody lower side, causing the pitching down moment and normal force to decrease. If the spouting jet angle is inclined further (below 60 deg in this study), pitching down moment generation due to the extended high-pressure region in front of jet nozzle causes the total pitching down moment to increase again.

Normal force becomes maximum when $\psi = 90$ deg, but decreases as spouting jet angle is inclined forward or backward because jet thrust decreases by cosine law. Therefore, selecting the proper

Fig. 11 C_p contour on surface, $\theta = 180$ deg.Fig. 12 C_N and C_M vs spouting jet angle.

spouting jet angle minimizes the pitching moment, while satisfying the required normal force for attitude control.

Optimal Design of the Lateral-Jet-Controlled Missile

Two types of missile attitude control using a lateral jet can be considered, as shown in Fig. 13. First, by the locating of the jet at the center of gravity of the missile, a parallel transition movement of missile (Fig. 13a) can be obtained by avoiding pitching moment generation. The other type is to control the missile attitude using the pitching moment generated by the jet located at a certain distance from the missile center of gravity (Fig. 13b). In this study, the former, a lateral jet located at the center of gravity, is considered. Therefore, the pitching moment generation, which is a negative effect on the missile control, should be diminished.

A numerical design optimization study for the effective flight condition is performed based on the results of the parametric study. The design problems are formulated by defining the design variables and the design constraints. With proven optimization and approximation techniques incorporated, the design optimization is performed at an altitude of 10 km. Pitching moment and normal force are selected

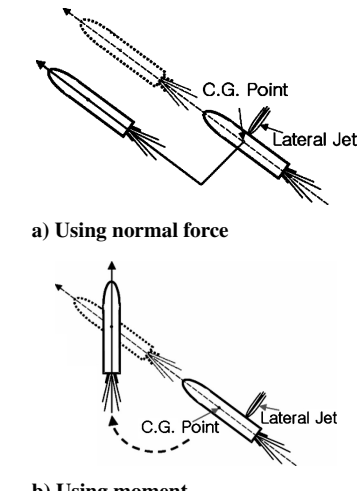


Fig. 13 Missile attitude control using lateral jet.

as the objective and constraint functions, respectively. Flight Mach number, angle of attack, and spouting jet angle are selected as design variables. The optimization also incorporates the response surface method.⁹

The optimization formulation is as follows: Minimize

$$F(X) = |C_{M_{\text{total}}}| \quad (4)$$

subject to

$$g(X) = 7C_{N_{IG}} - C_N \leq 0 \quad (5)$$

where

$$X = \{\alpha, \psi, M_\infty\}$$

$$-20 \leq \alpha \leq 20$$

$$30 \leq \psi \leq 90$$

$$2 \leq M_\infty \leq 4$$

$C_{N_{IG}}$ represents the normal force coefficient required to obtain initial 1-g acceleration for the missile transition without respect to drag. The assumed missile weight is 500 kg, jet Mach number is 2.0, and P_{ratio} is 150. The missile shape is identical to that used in the case studies.



Fig. 14 RSM.

Numerical Optimization Technique

The optimization algorithm implemented for this study is the genetic algorithm employed in GENOCOP III,¹⁰ developed by Michalewicz and others. A genetic algorithm simulates the Darwinian concepts of evolution and is an optimization technique based on stochastic search and natural selection. The operators used in a genetic algorithm are selection, crossover, and mutation. Selection determines the fitness of each individual. Crossover accelerates the convergence speed and transfers the gene with higher fitness to the next generation. Mutation helps to prevent a degenerate population, which tends to settle prematurely at a nonoptimal solution. A global search using the genetic algorithm is possible because it solely carries out an evolution of random tries by individuals without using gradient information.

System Approximation Using the Response Surface Method

The accuracy of the analysis can be improved by applying high-fidelity methods such as Navier-Stokes equations. However, the computational effort and cost involved are major hurdles in the design optimization process characterized by repetitive calculations. In spite of rapid growth in computational power, it may not be possible, when utilizing the conventional method, to obtain usable design solutions for many practical design and optimization problems within given time.

In this study, more than 6 CPU h are required for a single analysis using the Compaq Alpha workstation with 700-MHz processor for the numerical analysis of the detailed flowfields around the missile body and side jet. Therefore, it takes an unreasonable amount time to connect directly the computational fluid dynamics code and the optimizer because many analysis runs are required during the optimization process. This is especially significant when a genetic algorithm is employed, which requires more than 10,000 analysis calculations in most cases.

To reduce the huge computational loads, the response surface method, a popular technique in the multidisciplinary optimization studies, has been employed. The response surface method (RSM)⁹ is a statistical method, utilizing the design of experiment theory (Fig. 14). It generates a multidimensional surface (response surface) by making up an experimental model with obtained data to predict the response of the nonexperimented region. This method can approximate the global optimum by building the response surface according to the change in design variables. Generally, the second-order polynomial function about the design variables is used to represent the response surface,

$$y_{\text{predict}} = b_0 + \sum_{i=1}^k b_i x_i + \sum_{i=1}^k b_{ii} x_{ii}^2 + \sum_{i=1}^{k-1} \sum_{j=2}^k b_{ij} x_i x_j \quad (6)$$

where x_1, x_2, \dots, x_k are the design variables that affect the response, $b_i, i = 1, 2, \dots, (k+1)(k+2)/2$, are the coefficients of the regression function, and y_{predict} is the predicted value from the regression function.

The quality of the response surface generated using the experimental points can be estimated by the adjusted R^2 square, R_{adj}^2 (Ref. 9). R_{adj}^2 has values between 0 and 1. The generated response surface approaches 1 when it closely approximates the analysis results. Gen-

erally speaking, a response model fitting that has R_{adj}^2 above 0.9 can be regarded as reliable. The influence of the coefficients of the regression function can be estimated by T statistics. Coefficients with large T-statistics values have a strong influence on the entire response model. Coefficients with relatively small T-statistics values can be eliminated in generating the response model. The full regression model, which preserves all of the coefficients of the regression function, has been used in this study.

Design Optimization Strategy Using the RSM

The initial response surface is generated with a relatively small number of experiment points to minimize the number of analysis runs while maintaining the reliable regression model. Then, the optimum point obtained at a design iteration is added to the set of experimental points to generate a new regression model. This procedure is repeated until convergence. Usually 2–3 iterations are sufficient to obtain the converged optimum point. Because only one additional analysis run is required in each design iteration, considerable reduction of analysis runs can be expected.

In this study, the regression models are generated for the pitching moment (objective function) and the design constraint (the normal force). In general, 60% more experiment points than number of polynomial coefficients are required. In this study, three design variables are selected. Therefore, 16 experiment points are adequate for the regression model generation. Because low correlation exists between design variables and design sensitivities of the objective function, 35 initial experimental points are selected to generate a reliable response surface. As already explained, interim optimum points obtained during design iterations are added to build a better regression model. Three design iterations are required to obtain a satisfactory optimum solution.

Design Optimization Results

The response surfaces generated are shown in Fig. 15. The solid contour line represents positive pitching moment, whereas the dotted line represents the negative. The optimum lies in the border of solid and dotted contour lines.

The pressure contours of the baseline conditions and the optimum design at symmetry plane and at the missile surface are shown in Figs. 16 and 17, respectively. Baseline 1 is the case where the normal force is closest to that of the optimal shape among the initial experiment points. Thus, the improvement of the pitching moment characteristics of the optimum design can be compared. Baseline 2 is the flight condition that has the least pitching moment. Therefore, the normal acceleration capability of the optimum design can be compared.

From the case study in the foregoing section, the low-pressure region at the upper surface behind the nozzle is the primary cause for pitching moment generation. When the pressure distributions of baseline 1 and the optimum are compared, the latter has relatively small low-pressure region at the upper surface behind the nozzle.

Baseline 1 has a strong jet normal force by the normal spout jet angle, but a big loss is experienced because of the high angle of attack and the resulting bow shock. Therefore, both baseline 1 and the optimum have almost the same normal force. Baseline 2, which has zero angle of attack, experiences no normal force loss due to the

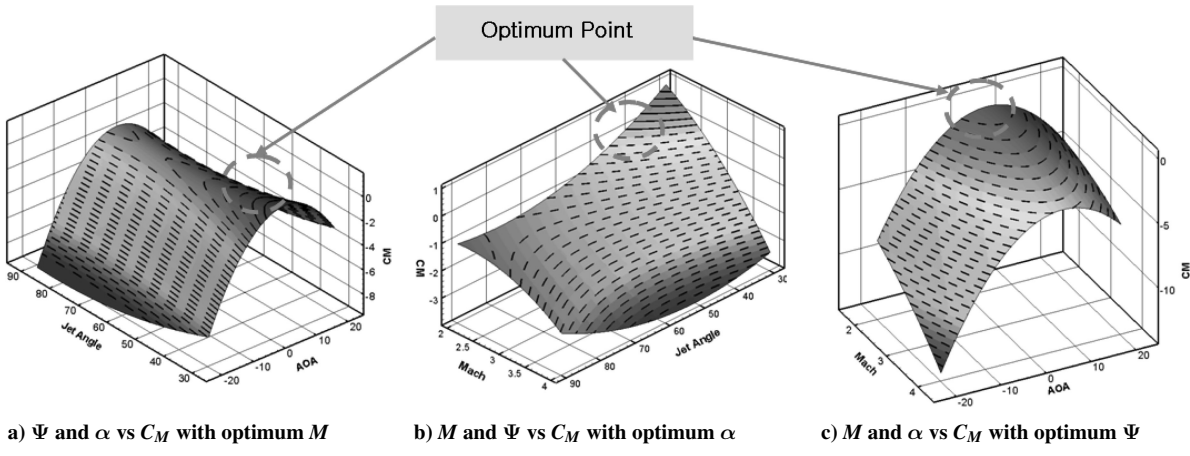


Fig. 15 Constructed response surface.

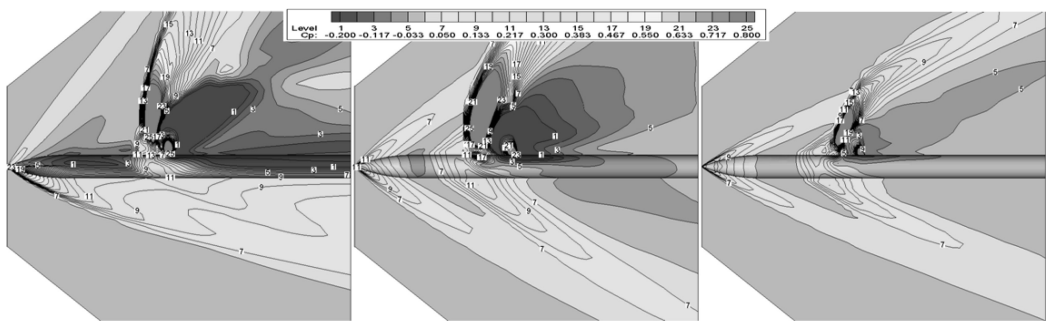
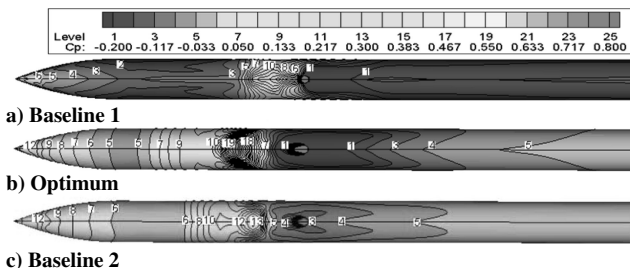
Fig. 16 C_p contour on symmetry plane.Fig. 17 C_p contour on surface.

Table 7 Optimization result compared with baseline 1

Case	α	ψ	M_∞	C_M	C_N
Baseline 1	20.0	90.0	2.0	-2.09	-6.36
Optimum	3.05	41.37	2.02	-0.14	-6.51
% Improvement	—	—	—	93.3	2.36

angle of attack. The jet spouting angle toward the upstream direction reduces the low-pressure region behind the nozzle. Therefore, baseline 2 has superior pitching moment characteristics among the initial experiment points.

The pitching moment and the normal force results of the baselines 1 and 2 and the optimum according to the angles of attack, spouting jet angles, and freestream Mach numbers are compared in Tables 7 and 8.

Compared to baselines 1 and 2, the optimum condition shows improved pitching moment and normal force characteristics. Most notably, the optimum shows 30% improvement in the normal force

Table 8 Optimization result compared with baseline 2

Case	α	ψ	M_∞	C_M	C_N
Baseline 2	0.0	30.0	3.0	-0.81	-5.03
Optimum	3.05	41.37	2.02	-0.14	-6.51
% Improvement	—	—	—	82.72	29.42

and 80% reduction in pitching moment when compared to baseline 2, the initial design with least pitching moment.

Conclusions

The flowfield around lateral-jet-controlled missile has been analyzed with respect to several freestream angles of attack and spouting jet angles. At relatively high negative angle of attack (around -20 deg in this study), large normal force loss and pitchdown moment are generated because the vortex bent by freestream extends the low-pressure region behind the jet nozzle. This results in abrupt decrease of the normal force and the increase of the pitchdown moment. Thus, high negative angle of attack should be avoided when a lateral jet is used during the missile operation. The pitchdown moment could be decreased by inclining the spouting jet angle forward, which results in low-pressure region reduction. However, excessively inclined spouting jet angle again causes pitchdown moment increment. Therefore, the pitchdown moment can be minimized by selecting the proper jet angle. The low-pressure region behind the jet nozzle significantly contributes to pitchdown moment generation. Therefore, for efficient lateral jet attitude control system design, it is necessary to investigate how to reduce the low-pressure region. Based on the result of the parametric study, design optimization of the lateral-jet-controlled missile has been successfully performed to minimize pitching moment while satisfying normal force constraint using a genetic algorithm and RSM.

References

- ¹Lacau, R. G., and Robert, M., The Use of Lateral Jet Control at Aerospatiale, *Proceedings of the Missile Aerodynamics Conference*, Nielsen Engineering and Research, Mountain View, CA, 1989, pp. 11-1–11-15.
- ²Billig, F. S., Orth, R. C., and Lasky, M., “A Unified Analysis of Gaseous Jet Penetration,” *AIAA Journal*, Vol. 9, No. 6, 1971, pp. 1048–1058.
- ³Brandeis, J., and Gill, J., “Experimental Investigation of Side-Jet Steering for Supersonic and Hypersonic Missiles,” *Journal of Spacecraft and Rockets*, Vol. 33, No. 3, 1996, pp. 346–352.
- ⁴Srivastava, B., “Computational Analysis and Validation for Lateral Jet Controlled Missiles,” *Journal of Spacecraft and Rockets*, Vol. 34, No. 5, 1997, pp. 584–592.
- ⁵Hoffmann, K. A., and Chiang, S. T., “Turbulent Flow and Turbulence Models,” *Computational Fluid Dynamics*, 4th ed., Vol. 3, Engineering Education System, Wichita, KS, 2000, pp. 20–115.
- ⁶Hirsch, C., “Second-order Upwind and High-resolution Schemes,” *Numerical Computation of Internal and External, Volume 2: Computational Method for Inviscid and Viscous Flow*, Vol. 2, Wiley, Chichester, Great Britain, U.K., 1984, Chap. 21, pp. 493–594.
- ⁷Yoon, S., and Kwak, D., “Three-Dimensional Incompressible Navier-Stokes Solver Using Lower–Upper Symmetric-Gauss–Seidel Algorithm,” *AIAA Journal*, Vol. 29, No. 6, 1991, pp. 874, 875.
- ⁸Perkins, E. W., and Jorgensen, L. H., “Comparison of Experimental and Theoretical Normal-Force Distributions (Including Reynolds Number Effects) on an Ogive–Cylinder Body at Mach Number 1.98,” NASA TN-3716, May 1956.
- ⁹Myers, R. H., and Montgomery, D. C., *Response Surface Methodology: Process and Product Optimization Using Designed Experiments*, Wiley, New York, 1995.
- ¹⁰Michalewicz, Z., *Genetic Algorithms + Data Structures = Evolution Programs*, 3rd ed., Springer-Verlag, New York, 1996.